



Shape Morphing Programmable Systems for Enhanced Control in Low-Velocity Flow Applications

Jin-Tae Kim, Taegeun Kim, Heesung Jung, Yu-Ting Huang, Youngmin Jeon, Fei Liu, Shyuan Cheng, Jaehong Park, Jeonhyeong Park, Ben Jeffery, Taehoon Kim, Xiaoyue Ni, Namjung Kim, Donghyun You,* Leonardo P. Chamorro,* Xinchen Ni,* and John A. Rogers*

Active flow control has gained substantial interest due to the ubiquitous role of fluids in engineering systems and applications and its potential to enhance aero-, hydro-, and hemodynamic system performance. This study presents an active flow control strategy employing a programmable shape-morphing system actuated by Lorentz forces in liquid metal-embedded microfluidics. The proposed system enables rapid, reversible, and three-dimensional deformations of a thin elastomeric membrane without the need for external flow sources or high-voltage inputs. The platform is evaluated for its capacity to induce distinct motions at various incoming velocities, revealing significant effects on momentum change. The study integrates advanced experimental techniques, reduced-order modeling, and state-of-the-art numerical methods to validate the system's versatility and performance. The findings highlight the potential of this soft actuating system to enhance flow control strategies, with potential applications ranging from improving the aerodynamics of bio-inspired flying sensors to mimicking natural locomotion mechanisms in low-velocity regimes. Further exploration of material innovations is crucial to expanding the system's capabilities and impact on specific flow control applications.

1. Introduction

In recent years, the demand for advanced flow control and modulation strategies has steadily increased, driven by objectives such as reducing drag of aerospace systems, [1,2] minimizing wall shear stress in hemodynamics, [3,4] and providing insights of fluid mechanics associated with active wall motions.^[5–7] Growing concerns over energy efficiency, health, and climate change have further highlighted the importance of efficient flow control and modulation, introducing new challenges in the field. Recent developments of passive flying sensors inspired by wind-dispersed seeds, known as "electronic fliers", further emphasize the significance of flow control strategies in low-velocity regimes. [8-12] In this class of flying sensors, maximizing airborne time or payload capacity is crucial for enhancing their ability to monitor environmental and atmospheric conditions. Various actuating

J.-T. Kim, T. Kim, Y. Jeon, D. You Department of Mechanical Engineering Pohang University of Science and Technology Pohang 37673, Korea E-mail: dhyou@postech.ac.kr

H. Jung, S. Cheng, L. P. Chamorro
Department of Mechanical Science and Engineering
University of Illinois
Urbana, IL 61801, USA
E-mail: lpchamo@illinois.edu

The ORCID identification number(s) for the author(s) of this article can be found under https://doi.org/10.1002/aisy.202500457.

© 2025 The Author(s). Advanced Intelligent Systems published by Wiley-VCH GmbH. This is an open access article under the terms of the Creative Commons Attribution License, which permits use, distribution and reproduction in any medium, provided the original work is properly cited.

[Correction added on 23 July 2025 after online publication: The twelth author's first name was corrected in this version.]

DOI: 10.1002/aisy.202500457

Y.-T. Huang, J. A. Rogers Querrey Simpson Institute for Bioelectronics Northwestern University Evanston, IL 60208, USA E-mail: jrogers@northwestern.edu

F. Liu Department of Electrical and Computer Engineering Princeton University Princeton, NJ 08544, USA

J. Park
Department of Materials Science and Engineering
Cornell University
Ithaca, NY 14853, USA

J. Park, B. Jeffery, X. Ni Department of Mechanical Engineering University of Texas at Dallas Richardson 75080, USA E-mail: xinchen.ni@utdallas.edu

T. Kim
Department of Mechanical System Design Engineering
Seoul National University of Science and Technology
Seoul 01811, Korea

www.advancedsciencenews.com



mechanics are employed in flow control applications, classified into three general categories: 1) fluidics, which utilize fluid injection or suction, 2) moving surfaces, involving a moving body within or near the boundary domain, and 3) plasma actuators, utilizing corona or dielectric barrier discharges.^[2] Among these, active flow control strategies using moving surfaces are particularly common due to their advantages, including the absence of an external flow source and a low input voltage requirement. This type of actuator includes vibrating ribbons,^[13,14] periodically moving diaphragms,^[15,16] rotating surface elements,^[17,18] and morphing surfaces.^[19] However, the rigidity and simplicity of the materials used in these actuators often restrict their geometric mode shapes, thereby limiting their adaptability and control performance during operation.

Recent advances in materials science and manufacturing technologies have enabled the engineering design of architectures capable of reversible and programmable shape-morphing (PS) systems. [20,21] These dynamic morphing systems have been applied to different applications, such as medical robots, [22] 4D electronics, ^[23] and deployable structures. ^[24] A range of active materials has been investigated, including liquid crystal elastomers, [25] responsive hydrogels, [26] and dielectric elastomers, [27] along with various shape-morphing schemes such as compressive buckling^[28] and origami/kirigami.^[29] Despite these efforts, many challenges remain in programmability, morphing speed, and shape continuity. In response to these obstacles, our recent works introduce systems that leverage the electromagnetic actuation of filamentary metal traces^[30] and liquid metal networks embedded in soft silicone microfluidic channels, [31] addressing many of these limitations. This system enables rapid, reversible shape-reprogramming among numerous complex and smooth 3D configurations, offering notable advantages in terms of speed, power consumption, and scalability without the need for the pumps and valves used in conventional pneumatically actuated systems. [31] Such a system has the potential for precise flow sensing and probing, leading to customizable flow control strategies.

One of the most common methods for active flow control relies on pressure-driven flow, such as syringe pumps, peristaltic pumps, or gas pressure regulators, which typically require input voltages of $\approx\!10\,\mathrm{V}$ and power consumption in the watts range. $^{[32]}$ In contrast, the PS system operates at $\approx\!60\,\mathrm{mW}$ per ribbon, offering a significantly lower power alternative. Micro-electro mechanical systems (MEMS)-based active wall motion techniques, such as piezoelectric actuators generating surface acoustic waves, operate at MHz-GHz frequencies but produce vibration amplitudes in the nanometer range. $^{[6,33]}$ By comparison, the PS system achieves millimeter-scale surface modulation. Another established method involves controlled localized heating to alter viscosity and surface tension for active flow control, but this approach typically requires seconds to minutes to reach target temperatures, $^{[34]}$ whereas the presented

X. Ni

Department of Mechanical Engineering and Materials Science Duke University Durham, NC 27710, USA

N. Kim
Department of Mechanical Engineering
Gachon University
Gyeonggi-do 13120, Korea

Table 1. Comparison of the PS system with conventional actuator systems.

	Our PS system	Conventional actuator systems
Power consumption	≈60 mW per ribbon	Pressure (air/gas): 7.7 W ^[32]
·	•	Pressure (dual channel): 1330 mW ^[32]
		Electroosmotic: 13 mW ^[32]
Amplitude	≈1 mm	$pprox$ 10 nm $^{[6,33]}$
Response speed	10 ms	$pprox$ 30 s (heating) $^{[34]}$

PS system responds within milliseconds. A comparative summary is provided in **Table 1**.

This article incorporates recently reported soft shapeprogrammable surfaces utilizing distributed Lorentz forces as the basis for manipulating near-wall flows in various scenarios. The platform is modified and systematically examined for suitable flow control applications by operating and examining the system's oscillatory modes and responses. The new features include: 1) deformation dynamics of the liquid metal embedded microfluidics in oscillatory modes determined by finite element analysis (FEA), 2) analytical solutions of second-order propagating deformation of the thin elastic membrane in oscillatory operations, 3) flow perturbations by the system at various incoming velocities, ranging from laminar to turbulent flows, 4) flow measurements using advanced flow experimental techniques, 5) flow characterization in spatial-temporal and spectral domains, 6) validation and interpretation of the induced flow characteristics through a state-of-the-art computational approach based on a grapic processing unit (GPU)accelerated numerical method, and 7) demonstration of the system's capability for continuous operation and scalability of multichannel configurations to support a wide range of flow control strategies.

2. Results and Discussion

2.1. Programmable Surface for Flow Control Applications

Figure 1 provides an overview of the concept, including mechanics of shape programmable surface (PS) materials and methods for flow control applications. The fast-response, soft, complex, and energy-efficient morphing system demonstrates significant potential for flow control, particularly in managing flow actuation (Figure 1A) or inducing distinct coherent motions across different incoming velocities. The system consists of thin, soft microfluidics structures filled with eutectic gallium-indium (EGaIn; 75% Gallium, 25% Indium by weight) as the skeleton network and a elastomeric membrane as the surface (Figure 1B; see Experimental Section). The magnetic field (B) generated by the magnet beneath the PS interacts with the electrical current flowing through the liquid metal channels, generating a Lorentz force, $F = L_{ch}$ (I × B), where L_{ch} is the channel length. This force deforms the liquid metal, which in turn exerts pressure on the attached membrane, enabling programmable membrane deformation. Durability tests for the PS system, conducted over 7000 cycles, demonstrate consistent performance without noticeable degradation. The temperature increase due to Joule heating remains below

.com/doi/10.1002/aisy.202500457 by Northwestern University Libraries, Wiley Online Library on [18/11/2025]. See the Terms and Conditions (https://

on Wiley Online Library for rules of use; OA articles are governed by the applicable Creative Commons

www.advancedsciencenews.com

www.advintellsvst.com

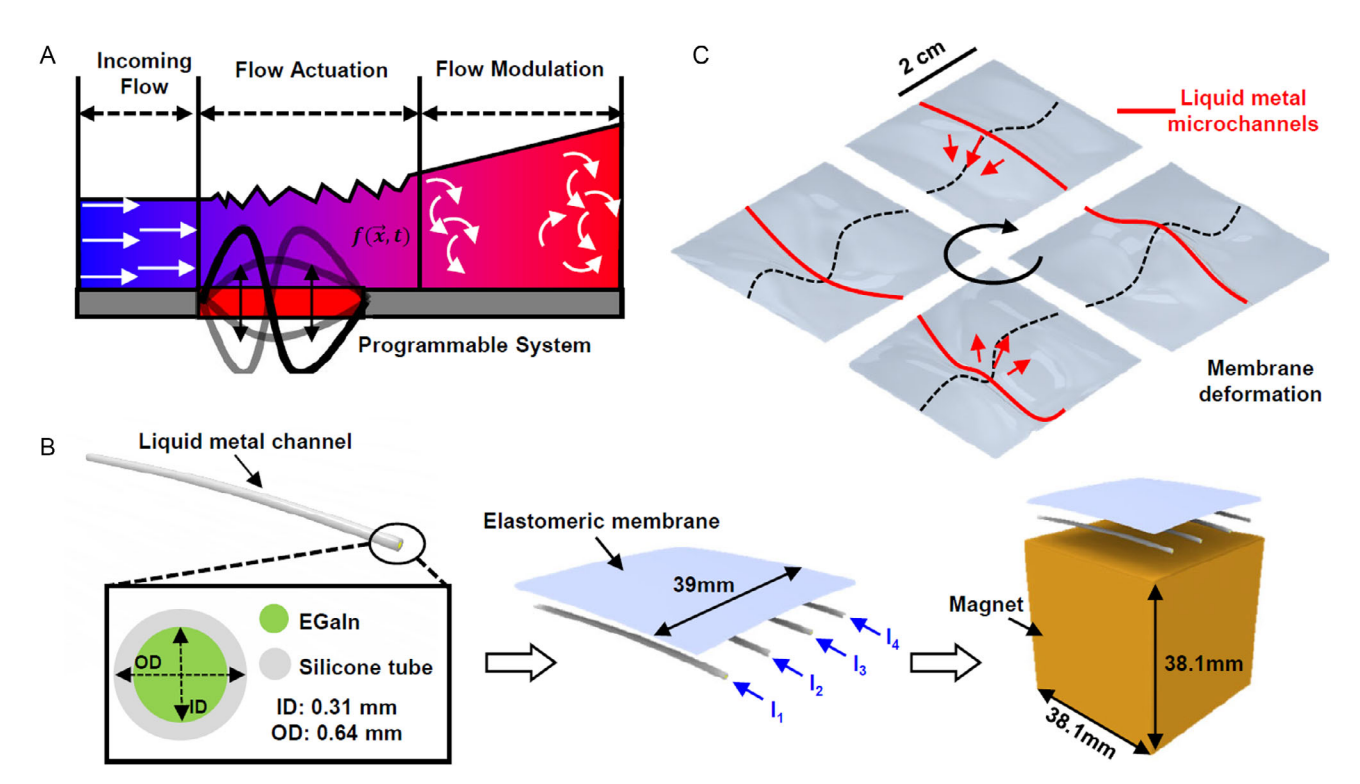


Figure 1. Programmable surfaces for flow control applications. A) Conceptual illustration of the programmable surface (PS) in a flow control application. B) Fabrication process of the PS. C) Schematic of the operation principle. Liquid metal-filled microfluidic channels are oscillated to generate secondary wavy deformations that propagate into a thin elastomeric membrane, forming the actuating surface.

 $5\,^{\circ}\text{C}$ at a current level of $\approx 0.5\,\text{A}$, indicating minimal thermal rise and rapid heat dissipation within the timescale of actuation, consistent with previous work. While prior research investigated the effects of ribbon layout and membrane thickness on static deformation. In contrast, this study emphasizes transient deformation and explores the underlying physics in oscillatory mode. A key feature of transient deformation is the second-order deformation, which becomes evident in oscillatory mode, as illustrated in Figure 1C and shown in Video 1, Supporting Information. This unique feature, coupled with an analytical solution, can be used as a facilitator in flow control strategies.

The response time of a liquid metal channel is investigated by an imaging method with a high-speed camera and validated by FEA (see Experimental Section), as shown in Figure 2A, left. The system exhibits a highly underdamped behavior with a stiffness-proportional damping factor $\beta = 5 \times 10^{-4}$, which is 20 times lower than the prediction reported in the previous work. When the system is operated at a frequency corresponding to resonant frequency ($f_c = 50 \text{ Hz}$), the peak deformation increases up to 5 mm, approximately doubling compared to continuous operation, while the power consumption decreases by the same factor due to oscillatory operation. This approach overcomes system limitations without altering the fabrication processes (Figure 2A, right; Figure 2B for raw images). With a resistance for each channel $R \approx 0.5\Omega$ and a current $I \approx 0.5A$, the average power consumption per ribbon per cycle is \approx 60 mW. The key physics of secondary deformations of the programmable surface induced by an oscillating metal channel can also be estimated considering theoretical arguments. For a simplified analysis,

the deformation of the surface is treated as a 2D standing wave with a rectangular boundary, estimated using a modified analytical solution based on Sturm-Liouville theory as follows

$$\gamma = \begin{cases} A \exp\left\{\zeta(x - x_c)\right\} \sin\left(\frac{\pi x}{2x_c} + \pi\right) \sin\left(\frac{\pi z}{L}\right) \sin\left(\frac{2\pi t}{T}\right), & \text{if } x < x_c \\ A \exp\left\{-\zeta(x - x_c)\right\} \sin\left(\frac{3\pi}{2(L - x_c)}(L - x)\right) \sin\left(\frac{\pi z}{L}\right) \sin\left(\frac{2\pi t}{T}\right), & \text{if } x > x_c \end{cases}$$

$$\text{if } x > x_c$$

$$(1)$$

where γ is the wall-normal displacement of the programmable surface, z is the coordinate in the spanwise direction, A is the channel amplitude, T is the period, L=40 mm is the length of the surface, $\zeta=0.5$ is the damping coefficient, and $x_c=3L/5$ is the streamwise location of the channel. Here, x=0 represents the leading edge and x=L the trailing edge of the PS. $A \propto iB/EI$ is proportional to the magnitude of the current, i, and the intensity of the magnetic field, B, measured by a magnetometer (MFM3000, PCE Instruments) and inversely proportional to the elasticity, E, and moment of inertia of the channel, I (see Experimental Section for details). The analytical results show reasonably good agreement with experimental results, thereby enabling its use for various design and flow scenarios (Figure 2C,D, Video 1, Supporting Information).

26404567, 2025, 11, Downloaded from https:

com/doi/10.1002/aisy.202300457 by Northwestern University Libraries, Wiley Online Library on [1811/12025]. Se the Terms and Conditions (https://online.library.wiley.com/terms-and-conditions) on Wiley Online Library for rules of use; OA article are governed by the applicable Creative Commons

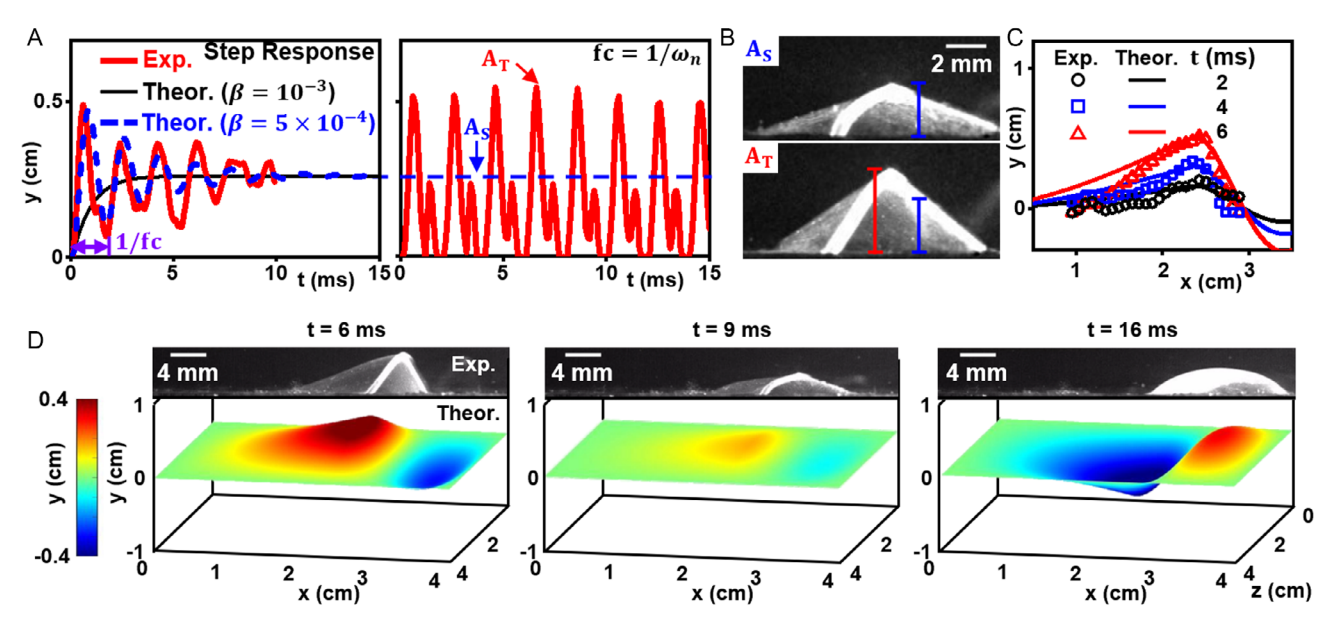


Figure 2. Experimental and analytical investigations of the dynamics of the programmable surface. A) (left) Step response of the PS with different Rayleigh damping factors compared to the experiment and (right) amplitudes of the PS during the static mode (A_5) and oscillatory mode (A_7). The amplitude increases by a factor of \approx 2 without modifying the fabrication process and system configuration. B) Raw images of the maximum amplitude during A_5 mode and A_7 mode. C) Comparison between experimental results and analytical modeling of the PS oscillation in 2D and D) same comparison in 3D.

2.2. Programmable Surface Performance Across Flow Regimes

The performance of the PS under various incoming velocities was experimentally characterized by time-resolved particle image velocimetry (PIV) with a sampling rate of 1,000 Hz in a customized wind-tunnel (Figure 3A and S1, Supporting Information) with the channel width $L_{Channel} = 45$ mm (see Experimental Section for details). The flow characteristics modulated by PS are analyzed primarily in the near field, from 1 L to 3 L downstream to minimize potential 3D and wall effects in the far field. The PIV system consisted of a 2 megapixel Emergent HT-2000M high-speed camera equipped with a 50 mm F1.4 manual-focus Kowa lens, a laser pulse synchronizer (Model 610036, TSI), and PIV control software (PIVlab). [35] A planer laser sheet illuminated the center of the wind tunnel behind the programmable surface (PS), where the field of view covered a $30 \, \text{mm} \times 80 \, \text{mm}$ region. To ensure accurate flow tracking, oil droplets (≈1 to 5 µm in diameter) were used as tracer particles, yielding a Stokes number (Stk) $\ll 1$. The camera captured over 5,000 frames at a sampling frequency of 1,000 Hz. The image sequences were processed using direct Fourier transform correlation. The final interrogation window size was 16 pixels × 16 pixels with 50% overlap, resulting in a vector grid spacing of 0.62 mm along both x and y axes with over 95% of velocity vectors resolved.

Two sets of experiments conducted: one with PS modulation at the resonant frequency, $f_c = 50 \mathrm{Hz}$, and the other without modulation, f_0 . These are performed at three incoming velocities, $U = [0.65, 1.06, 1.49] \ \mathrm{m \, s^{-1}}$ (Video 2, Supporting Information). The selected velocity range corresponds to the mechanisms of airborne seed dispersal, spanning from parachuting seeds (e.g., dandelion seeds) to autorotating seeds (e.g., maple seeds). [8] This range is chosen to highlight the PS system's capability to generate distinct coherent motions under controlled conditions at low incoming

velocities, which are relevant for flow control applications in bioinspired flying sensors. At higher incoming velocities, flow instabilities can be more easily triggered with minimal actuation. Therefore, using relatively low incoming velocities emphasizes the actuator's capability to generate and sustain meaningful flow perturbations in a regime where external instabilities are minimal or nondominant. It is worth noting that these investigations focus on the performance of the PS operated at its resonant frequency, underscoring its potential and distinct effects on the flow. Additional experiments with the PS at various frequencies show good agreement with the step response results in Figure 2A. For instance, at 100 Hz, a frequency higher than the resonant, the PS exhibits a significant decrease in amplitude (Video 3, Supporting Information). Addressing the complex nonlinear interactions and instabilities inherent in near-wall dynamics, particularly those associated with operation at various frequencies, is beyond the scope of this work.

A basic assessment of the flow patterns and coherent motions induced by the PS is given based on the time-averaged velocity distribution in Figure 3B (Video 4, Supporting Information for time-dependent PIV results). The cases without PS modulation (f_0) exhibit typical boundary layer flow over a flat surface with the velocity gradient near the surface following the Blasius relation, $\delta \propto \sqrt{vx/U}$, where δ is the boundary layer thickness, highlighting consistency between experiments and established flow behavior (Figure 3B, left and Figure S2A, Supporting Information). However, the flow characteristics induced by PS oscillation reveal significant modulations near the surface, with noticeable streamwise propagation, particularly at $U = 1.06 \text{ m s}^{-1}$ and 1.49 m s⁻¹, indicating emerging instability (Figure 3B, right). The impact of PS modulation on the boundary layer is further characterized by examining mean streamwise velocity, \overline{u} , (Figure 3C), standard deviation of the velocity fluctuations, σ_u , (Figure S2B,

26404567, 2025, 11, Downloaded from https

.com/doi/10.1002/aisy.202500457 by Northwestern University Libraries, Wiley Online Library on [18/11/2025]. See the Terms and Conditions (https://onlinelibrary.wiley.com.

conditions) on Wiley Online Library for rules of use; OA articles are governed by the applicable Creative Commons

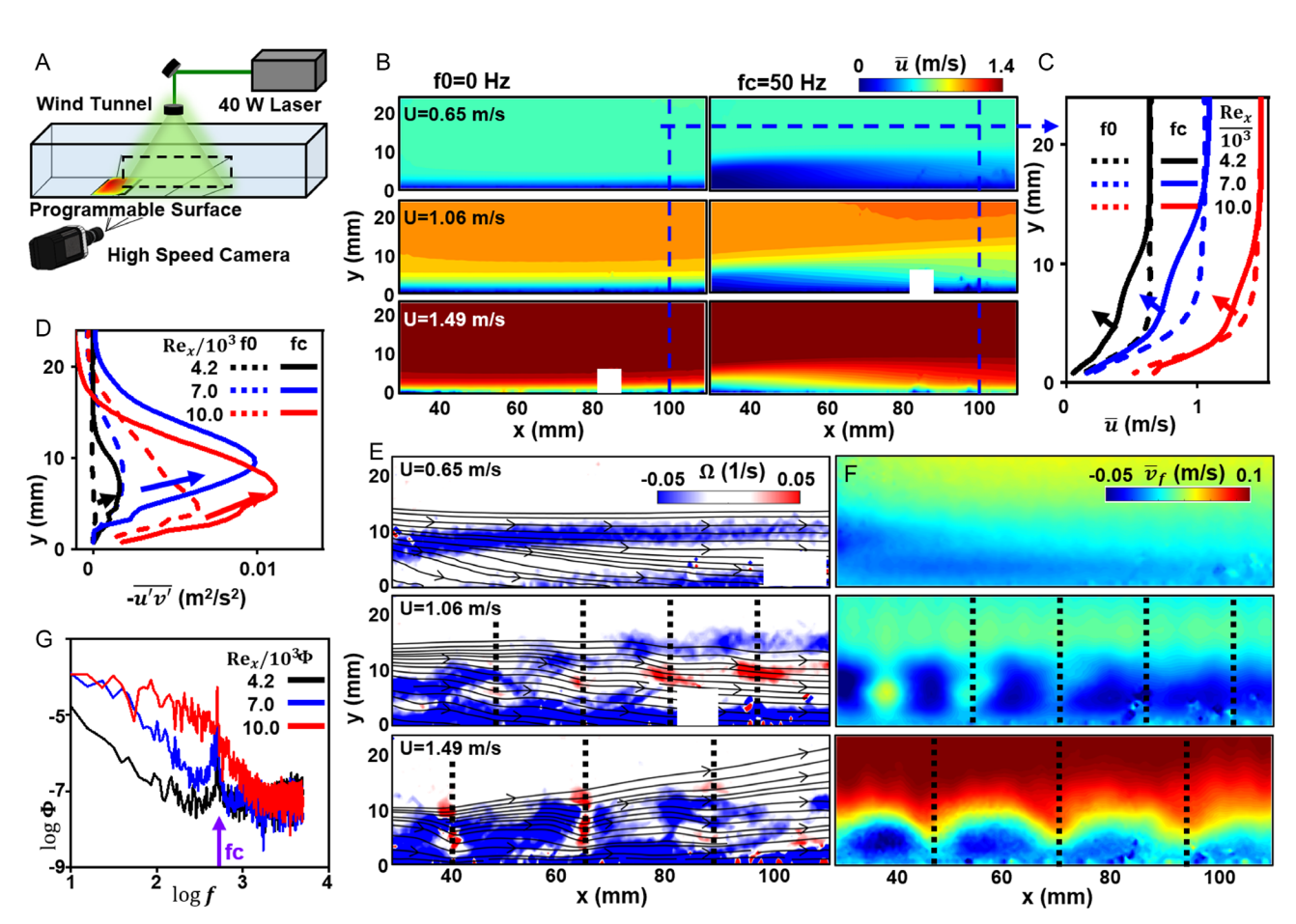


Figure 3. Programmable surfaces versus incoming velocities. A) Experimental setup for the PIV measurements of the flows modulated by the PS system. B) Mean streamwise velocity distributions for the null cases, $f_0 = 0$ Hz, (left) and PS modulated cases (right) operated at the natural frequency, $f_C = 50$ Hz. Top, middle, and bottom contours indicate different incoming velocities at U = [0.65, 1.06, 1.49] m s⁻¹. White masks in the contour maps indicate noise, which was filtered out during preprocessing to enhance the data reliability. C) Velocity profile comparisons between f_0 and f_C cases at x = 100mm downstream. D) Reynolds shear stress comparisons between f_0 and f_C cases at x = 100mm downstream. E) Instantaneous vorticity fields, $\Omega = \frac{dy}{dy} - \frac{du}{dy}$, for f_C cases at various incoming velocities. F) Phase-averaged spanwise velocity distributions at various incoming velocities. Vertical dotted lines illustrate the location of vortical structures. G) Power spectra of the streamwise velocity at x = 100 mm and y = 4 mm for the PS modulated cases under various incoming velocities.

Supporting Information), and Reynolds shear stress, $\overline{u'v'}$ (Figure 3D) profiles at x=100 mm downstream for each incoming velocity, corresponding to the local Reynolds number $Re_x=Ux/v$ of $[4.2, 7.0, 10.0] \times 10^3$, where $v=1.5 \times 10^{-5}$ m² s⁻¹ is the kinematic viscosity of air.

Here, u and v denote the streamwise and wall-normal velocity components, decomposed into their time-averaged and fluctuating components as $u=\overline{u}+u'$, and $\overline{u'v'}$ describes turbulent momentum transfer. It is worth noting that significant momentum deficits occur around $2 < \gamma < 12$ mm, corresponding to the outer layer, across all cases (Figure 3C). The outer layer, primarily governed by inertial forces, is positioned above the inner layer, where viscous effects play a critical role. The results confirm that PS modulation induces distinct inertial forcing that significantly alters the outer region. Specifically, the modulated boundary layer profiles exhibit characteristics akin to an adverse pressure gradient condition, marked by an inflection point indicative of potential flow separation. This feature could be leveraged to

actively control separation points on flying sensor's surfaces, thereby optimizing aerodynamic performance. The pronounced increase in Reynolds shear stress within the same region further supports this argument (Figure 3D). Further discussion on the flow characteristics and induced dominant coherent motions analyzed using reduced-order decomposition techniques can be found in Supplementary Note I, Supporting Information. It is important to emphasize that the desired effects on the flow depend on several key parameters, including the boundary layer thickness of the incoming flow, the local pressure gradient, background turbulence, and other contributing factors. Within these considerations, the proposed PS system offers the versatility to tailor and optimize its impact on the flow, providing a customizable solution for a wide range of flow control applications.

Frequency control of the PS modulation (PSM) is particularly critical in managing flows within the spatiotemporal domain. This control influences the evolution of coherent vortical structures across multiple scales, as illustrated in the instantaneous

ADVANCED INTELLIGENT SYSTEMS

www.advancedsciencenews.com www.advintellsyst.com

vorticity fields (Figure 3E). The flow downwind of the PS system at $U = 0.65 \text{ m s}^{-1}$ exhibits a stable shear layer characteristic of low-Reynolds-number flow. In contrast, the higher incoming velocity cases exhibit prominent vortical structures with distinct spatial patterns of velocity shear, resembling Kelvin-Helmholtztype instability. The perturbations and vortices are consistent downwind, as shown in the phase-averaged velocity distribution (Figure 3F). The streamwise velocity spectra (Figure 3G) illustrate the energy distribution and transfer mechanisms. The spectrum displays a -5/3 scaling, defining the inertial subrange with the higher incoming velocity case, which describes higher energy across scales. Across all incoming velocities, distinct spectral peaks emerge at the PS modulation frequency, f_c , indicating that the PSM effectively injects energy at a controlled frequency, compared to the null cases (Figure S2C, Supporting Information), thereby influencing flow behavior in both the spatial and temporal domains (see Supplementary Notes I, Supporting Information for details on reduced order modeling).

2.3. Computational Approach

Direct numerical simulations, based on a GPU-accelerated computational method^[36] using three Tesla P100 GPUs, are conducted by numerically solving the nondimensional incompressible Navier–Stokes equations to characterize associated flow patterns and implement a future modeling capability of the

system. A second-order central difference scheme on a staggered grid is used to calculate the spatial derivatives. Time marching is conducted using a semi-implicit fractional-step method, which implicitly integrates the diffusion terms with the Crank–Nicolson scheme and explicitly advances the convection terms with the third-order Runge–Kutta scheme^[36] (see Experimental Section for details). The deformation of the PS is implemented using two different numerical approaches. Both approaches consider wall-normal displacement of the PS as a boundary condition in the simulation by using sinusoidal functions.

In the first approach, the deformation in the spanwise and streamwise directions is considered, denoted as the three-dimensional surface oscillation. Figure 4A shows the contours of instantaneous streamwise velocity for $U=1.06~{\rm m\,s^{-1}}$. Circular-shaped velocity patterns appear alternatively and periodically for $\gamma>10~{\rm mm}$, similar to the experimental results. The three-dimensional nature of this phenomenon is highlighted through the iso-surfaces of nondimensionalized Q-criteria, as shown in Figure 4B (Figure S3, Supporting Information for the case of $U=1.06~{\rm m\,s^{-1}}$). Ring-shaped vortical structures appear periodically with similar length scales of the PS oscillations. These structures are stretched in the spanwise direction toward downstream and are maintained at the end of the simulation domain.

In the second approach, denoted as the two-dimensional surface oscillation, only wall-normal displacement of the PS is considered since the deformation in the spanwise direction is negligible due to its small displacement. The mean velocity

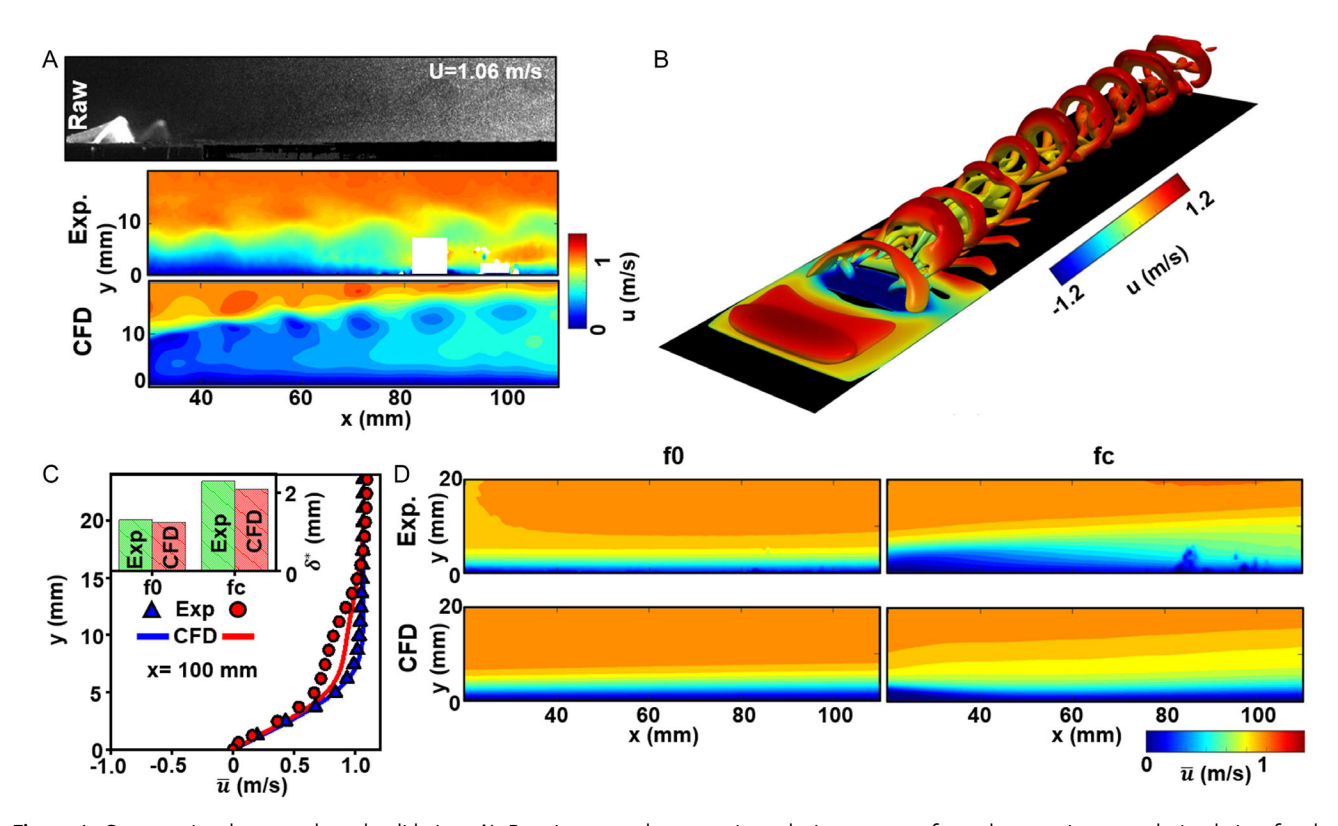


Figure 4. Computational approach and validation. A) Raw image and streamwise velocity contours from the experiment and simulation for the representative instant. White masks in the contour maps indicate noise, which was filtered out during preprocessing to enhance the data reliability. B) Iso-surface of nondimensional Q-criterion at the representative instant. C) Mean velocity profiles at x = 24mm, comparing the experiment and simulation. D) Mean streamwise velocity contours, comparing f_0 and f_C cases from the experiment and simulation.

elibrary.wiley.com/doi/10.1002/aisy.202500457 by Northwestern University Libraries, Wiley Online Library on [18/11/2025]. See the Terms

on Wiley Online Library for rules of use; OA articles are governed by the applicable Creative Commons

profile of the simulation at x = 100 mm downstream for the case of $U = 1.06 \,\mathrm{m\,s^{-1}}$ (Figure 4C) is compared with that of the PIV measurement. A similar level of momentum deficits is observed in the experiment and simulation based on the momentum thickness, $\delta^* = \int \frac{u}{U} (1 - \frac{u}{U}) dy$ (Figure 4C, inset). Potential sources of the discrepancy observed in Figure 4C may include the presence of higher-order structural vibrations of the PS in the experiment and slight variations in inflow conditions between the experiments and simulations. Figure 4D shows the contours of mean streamwise velocity from the experiment and simulation, indicating relatively good agreement in capturing overall changes in wall-bounded flow characteristics (see Supplementary Notes II, Supporting Information for details). It is worth noting that higher-order flow phenomena, including the characteristics of turbulent boundary layers and the spatial intermittency regime, are beyond the scope of this study.

2.4. Amplitude and Frequency Controllability

Establishing the PS system through analytical, experimental, and computational methods offers an effective real-time morphing scheme to continuously alter wall-bounded flows with controllable capability in both magnitude and frequency. Figure 5A demonstrates the time evolution of streamwise and spanwise

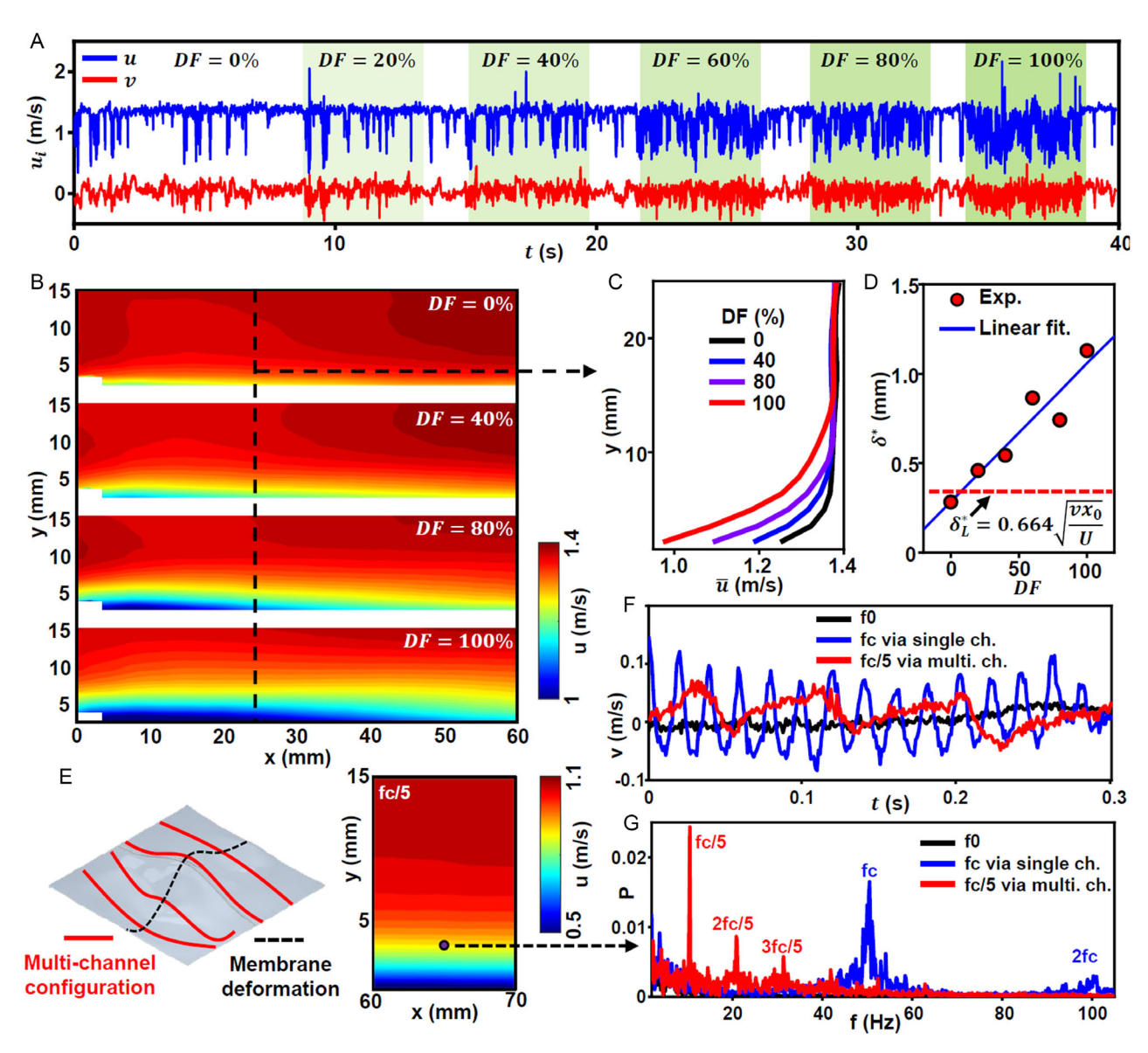


Figure 5. Amplitude and frequency controllability. A) Time evolution of the streamwise velocity at x = 24mm and y = 4mm during continuous operation with varying duty factor (DF). B) Time-averaged streamwise velocity distributions at various DF. C) Velocity profiles at x=24mm at various DF. D) Momentum thickness, $\delta^* = \int \frac{u}{l!} (1 - \frac{u}{l!}) dy$, with resect to DF. E) Illustration of a multichannel configuration (left) and mean streamwise velocity distribution of the multi-PS system operated at $f_C/5$ (right). F) Streamwise velocity comparison in the temporal domain. G) Streamwise velocity comparison in the spectral domain at x = 65mm and y = 4mm between the single-channel configuration operated at f_c (blue) and the multichannel configuration operated at $f_C/5$ (red).

ADVANCED Intelligent Systems

www.advintellsyst.com

www.advancedsciencenews.com

velocities in the outer layer ($x = 24 \,\mathrm{mm}\,\mathrm{and}\,\gamma = 3.6 \,\mathrm{mm}$) over 4.0×10^4 frames with various duty factors (DF), the ratio between the pulse duration and the period, of the PS system at $U = 1.06 \,\mathrm{m\,s^{-1}}$. As the DF increases, the amplitude of fluctuating components (i.e., vortical structures induced by the PS) also increases. The time-averaged velocity distributions (Figure 5B) and velocity profiles (Figure 5C) with respect to DF indicate a systematic change in momentum deficit as a function of DF. The momentum thickness (δ_I^*)increases linearly with the given DF. Starting near the momentum thickness of otherwise undistributed nearly laminar flows ($\delta_L^* = 0.664 \sqrt{vx/U}$ at zero DF), δ^* increases progressively, reaching up to 4 δ_I^* at 100% DF. The corresponding momentum thickness Reynolds number, Re_{δ} , indicates that PM modulation increases Re_{δ} by the same factor as δ_{I}^{*} under identical incoming velocity conditions (Figure S4, Supporting Information). As Re_{δ} is linked to drag, this feature can potentially enhance the capacity of electronic fliers for extended airborne time or increased payload weight.

Efficient control of boundary layer flows in the spectral domain can be achieved by implementing an N-by-N array of microfluidic ribbons, which mitigates the unwanted secondorder deformation of the elastomeric membrane. A 4-by-1 array of the PS has been developed, with each ribbon individually controlled and oscillated at a frequency five times lower than the system's natural frequency, $f_c/5$ (Figure 5E, left). The results demonstrate that the velocity distribution (Figure 5E, right) and velocity profile at a representative point (Figure 5F in the temporal domain and Figure 5G in the spectral domain) exhibit a similar magnitude of momentum deficit compared to the case at f_c , but the modulation frequency aligns with the operating frequency in a multichannel mode. The system's versatility in flow control applications, tested with various incoming flow conditions, amplitudes, and frequencies, suggests significant potential for this shapemorphing system in controlling directionality and geometrical aspects to manipulate the wall-bounded flows in various scenarios.

3. Conclusion and Outlook

Adv. Intell. Syst. 2025, 7, 2500457

This study introduces a versatile and robust design for PS systems, demonstrating their capability to manipulate near-wall flows across various scenarios. By leveraging these capabilities, the system can serve as a valuable tool for advancing flow control strategies, with practical applications that span both scientific exploration and engineering development. The Lorentz-forcedriven liquid metal-embedded microfluidic structures, integrated with a thin elastomeric membrane, provide capabilities previously unattainable in active flow control systems. This soft actuated system operates efficiently without requiring external flow sources or high-voltage inputs, enabling rapid and complex actuation with low power consumption. The work presented here serves as a demonstration of the programmable surface's potential to induce distinct flow perturbations and coherent motions, rather than as a comprehensive solution to the broader flow control paradigm. The secondary deformations of the programmable surface, observed experimentally and supported by analytical and numerical methods, illustrate its versatility in influencing boundary layer dynamics. By modulating PS properties and flow parameters such as amplitude, frequency, and incoming velocity, the system demonstrates systematic effects on momentum redistribution and outer-layer flow characteristics. These observations suggest potential applications in controlling flow separation, recirculating points, and coherent vortical structures intargeted scenarios. While the results highlight the system's capability to stabilize shear layers or induce flow instabilities like Kelvin–Helmholtz modes, the primary aim of this study is to showcase the flexibility and functionality of the programmable surface as a core platform.

This platform holds significant potential for advancing fundamental studies in flow control applications, such as active control of large-scale motions, [37] transition dynamics, [38] turbulence generation,[39] added mass,[40] and drag reduction.[41] The demonstration of this flexible morphing platform opens pathways for advanced flow-related phenomena, including wall modulation of dimensionality, [42,43] permeability, [44,45] and directionality. [46] Numerous opportunities exist for system improvement, particularly through material innovations. For example, incorporating thermo- or magnetic-responsive materials could enable multimodal, closed-loop control while facilitating the design of 3D morphable structures. Also, integrating microscale, mechanically supported 3D structures could provide precise programmability, extending the platform's influence across the entire range of wall-bounded fluid dynamics, from the viscous sublayer up to the outer layer. The system's flexibility and low power consumption could facilitate the emulation of various aerohydrodynamic bio-locomotion mechanisms—such as the side-to-side fish swimming or the up-and-down bird flight—highlighting its potential to inspire innovative approaches in flow modulation.

4. Experimental Section

Fabrication of Elastomeric Membrane: Preparation of an elastomeric membrane began by spin-coating (3000 rpm for 30 s) a thin layer of poly(4-styrenesulfonic acid) sol (PSS) onto a clean glass slide (75 mm \times 50 mm), which served as a sacrificial layer. The coated PSS layer was then cured at 180 °C on a hotplate for 5 min. Next, a soft silicone elastomer (Ecoflex 00-20) was spin-coated at 6000 rpm for 60 s onto the PSS layer and cured in an oven at 75 °C for 30 min, to yield a thin elastomeric membrane (thickness = $\approx 50~\mu m$). To provide structural support and facilitate handling, a 3D-printed frame (thickness = 8 mm, printer: Form 3, Formlabs, material: Flexible 80 A) was attached to the elastomeric membrane using an adhesive. To release the membrane from the glass slide, the entire assembly was submerged in water heated in a 75 °C oven for 20 min. This immersion process dissolved the underlying PSS, allowing for easy removal of the membrane with the attached frame.

Analytical Modeling and FEA: FEA simulations were conducted using an in-house MATLAB code to predict the static and dynamic deflection of the microchannel under Lorentz force. The microchannel is modeled as the Euler-Bernoulli beam with spatial discretization ($N_{element} = 100$) due to the microchannel's small deformation (≈3 mm) relative to the length (pprox48 mm). The Newmark time integration scheme is employed to explain the transient behavior of the microchannel. The homogeneous parameters for the Euler-Bernoulli beam are determined utilizing the liquid metal density ($\rho_{metal}=6.25\,\mathrm{g/cm^3}$), microchannel wall density ($\rho_{walls}=1.07\,\mathrm{g/cm^3}$), EGaIn stiffness ($E_{GaIn} = 210 \, \text{kPa}$), gallium stiffness ($E_{Gallium} = 9.8 \, \text{GPa}$), and microchannel wall stiffness ($E_{walls} = 232 \, \text{kPa}$). The liquid metal was assumed to behave as an incompressible solid, given its full sealing within microfluidic channels during the deformation. The averaged stiffness of liquid metal ($E_{liquidmetal} = 408 \text{ kPa}$) is calculated based on the weight percentage of EGaIn (25%) and Gallium (75%). The density of the microchannel ($\rho_{microchannel} = 1.93 \, \mathrm{g/cm^3}$) were computed based on the cross-sectional areas that were taken by the walls of microchannel and liquid

www.advancedsciencenews.com



www.advintellsvst.com

metal. The moment of inertia (I_{beam}) was determined as the sum of the moments of inertia of the microchannel wall (I_{wall}) and the liquid metal ($I_{liquidmetal}$), weighted by a factor, w=40. Additionally, Rayleigh damping, with a stiffness-proportional damping factor ($\beta=0.0005$), was used to account for dissipation effects of the liquid metal and viscous damping behavior of the microfluidic channel. The stiffness-proportional damping factor is carefully chosen to simulate the transient behavior of microchannel, as shown in Figure 1C.

A simple analytical modeling for estimating the amplitude of the channel, A, in a dynamic mode was derived as follows. The deflection profile of a fixed-fixed channel under a distribution force, F, is given by

$$A = -\frac{Fx}{24E_{heam}I_{heam}}(x^3 - 2Lx^2 + L^3)$$
 (2)

The maximum deflection occurs at the center of the channel, expressed as

$$A_{S} = -\frac{5FL^4}{384E_{beam}I_{beam}} \tag{3}$$

Given that the distributed force is the Lorentz force per unit length, F = iB, the maximum static deflection can be expressed as

$$A_{S} = -\frac{5iBL^4}{384E_{beam}I_{beam}} \tag{4}$$

For the dynamic case, the maximum deflection at the center of the channel in the first mode can be expressed as

$$A_T = \frac{A_5}{\rho_{microchoungl}S({\omega_1}^2 - {\omega^2})} \tag{5}$$

where S is the cross-sectional area of the channel, w_1 is the first-mode resonant frequency, and w is a given frequency. For simplicity, A_T is assumed as a value with weighting factor, proportional to the magnitude of the current and the intensity of magnetic field, and inversely proportional to the elasticity and moment of inertia of the channel. The weighting factor k is derived from the experimental result.

$$A_{T} = k \frac{iB}{FI} \tag{6}$$

 $A_T=f(x)$ is assumed to be the maximum amplitude at the resonant frequency oscillation, independent to time, and move only in the wall-normal direction.

A Customized Wind Tunnel: A customized wind tunnel was made of 1/8" thickness acrylic sheets, a 120 by 120 mm² fan (9G1212M1021 San Ace 120, Sanyo Denki America, Inc), 3D-printed flow straightener, and contraction cone. Acrylic sheets were cut by a CO² laser cutter (Universal Laser, VLS3.60) and assembled with the test section of $500 \times 45 \times 45 \text{ mm}^3$ using acrylic glue. The honeycomb-shaped flow straightener and bell-shaped contraction cone were printed using FDM 3D printer (Ultimaker S3) with the shared dimension of $50 \times 155 \times 155 \text{ mm}^3$. The flow straightener was designed as a grid structure of repeated 8 mm diameter hexagons to straighten and smooth the airflow. Oil droplets were injected behind the fan using a nebulizer. The contraction cone was designed to accelerate and streamline the airflow into the test section.

Computational Fluid Dynamics: The simulation is conducted by numerically solving the nondimensionalized incompressible Navier–Stokes equations as follows

$$\frac{\partial u_i}{\partial x_i} = 0 \tag{7}$$

$$\frac{\partial u_i}{\partial t} + \frac{\partial u_i u_j}{\partial x_j} = -\frac{\partial p}{\partial x_i} + \frac{1}{Re_{\delta_0^*}} \frac{\partial^2 u_i}{\partial x_j \partial x_j}$$
(8)

where t is the time, and x, y, z (= x_i) are the streamwise, the wall-normal, and the spanwise directions, respectively. The displacement thickness

Reynolds number is defined as $Re_{\delta_0^*} = U_\infty S_0^* / \nu$ based on the reference scales which are chosen as the inlet displacement thickness δ_0^* , kinematic viscosity ν , and the free stream velocity U_∞ . The velocity components $u, \nu, w \ (=u_i)$, and the pressure p are nondimensionalized using the reference scales δ_0^* and U_∞ . The reference scales of the boundary layer are calculated based on the Blasius boundary layer theory as provided in Supplementary Note II, Supporting Information.

The schematic of the computational domain is shown in supplementary Figure 1. There are two approaches to implement the deformation of programmable surface into the simulation as a boundary condition. In the first approach, the deformation of the programmable surface is considered in the spanwise direction and the streamwise direction. The schematic of the wall-normal displacement of the programmable surface is presented in supplementary Figure 4. The wall-normal velocity of the fluid on the programmable surface is assumed to be the same as the velocity of the surface. Therefore, the time derivative of the displacement is implemented in the simulation as a boundary condition.

$$\frac{dy}{dt} = \begin{cases} \frac{2\pi A}{T} \exp\left\{\zeta(x - x_c)\right\} \sin\left(\frac{\pi x}{2x_c} + \pi\right) \sin\left(\frac{\pi z}{L}\right) \cos\left(\frac{2\pi t}{T}\right), & \text{if } x < x_c \\ \frac{2\pi A}{T} \exp\left\{-\zeta(x - x_c)\right\} \sin\left(\frac{3\pi}{2(L - x_c)}(L - x)\right) \sin\left(\frac{\pi z}{L}\right) \cos\left(\frac{2\pi t}{T}\right), & \text{if } x > x_c \end{cases}$$

$$(9)$$

In the second approach, only wall-normal displacement of the programmable surface is considered (i.e., the deformation is denoted as two-dimensional surface oscillations). The displacement of the programmable surface is represented as follows

$$y = A\sin\left(\frac{2\pi}{T}t\right)\sin\left\{\frac{2\pi}{L}(x - x_{LE})\right\}$$
 (10)

where x_{LE} is the distance from the inlet to the leading edge of the programmable surface. The schematic of the wall-normal displacement of the programmable surface is presented in supplementary Figure 3a. Similar to the three-dimensional programmable surface case, the time derivative of the displacement is implemented in the simulation as a boundary condition.

$$\frac{d\gamma}{dt} = \frac{2\pi A}{T} \cos\left(\frac{2\pi}{T}t\right) \sin\left\{\frac{2\pi}{L}(x - x_{LE})\right\}$$
(11)

Details of boundary conditions and domain size are presented in supplementary note. The number of the grid points for the simulation is 720 \times 192 \times 128 in the streamwise, the wall-normal, and the spanwise directions, respectively. Grid spacings in the streamwise and the spanwise directions are uniform, while the wall-normal grid spacing follows a nonuniform profile. [47]

Supporting Information

Supporting Information is available from the Wiley Online Library or from the author.

Acknowledgements

J.-T.K. acknowledges that this work was supported by the National Research Foundation of Korea (NRF) and grant funded by the Korea government (MSIT) (RS-2024-00342270).

Conflict of Interest

The authors declare no conflict of interest.

on Wiley Online Library for rules of use; OA articles are governed by the applicable Creative Commons

www.advancedsciencenews.com www.advintellsyst.com

Author Contributions

Jin-Tae Kim, Xinchen Ni, Leonardo P. Chamorro, and John A. Rogers conceived the ideas and designed the research. Xiaoyue Ni, Yu-Ting Huang, Fei Liu, Jaehong Park, Jeonhyeong Park, and Ben Jeffery fabricated the shape-morphing systems. Jin-Tae Kim and Namjung Kim developed the analytical modeling of the mechanics. Namjung Kim performed FEA analyses. Jin-Tae Kim, Heesung Jung, and Shyuan Cheng performed and analyzed flow experiments. Taehoon Kim, Youngmin Jeon, and Donghyun You performed computational fluid dynamics. Jin-Tae Kim, Taegeun Kim, Heesung Jung, Leonardo P. Chamorro, Xinchen Ni, and John A. Rogers wrote the manuscript with input from all authors. Jin-Tae Kim and Taegeun Kim contributed equally to this work.

Data Availability Statement

The data that support the findings of this study are available in the supplementary material of this article.

Keywords

flow control, shape morphing materials, soft electronics

Received: April 25, 2025 Revised: July 5, 2025 Published online: July 21, 2025

- [1] D. Greenblatt, D. R. Williams, Ann. Rev. Fluid Mech. 2022, 54, 383.
- [2] L. N. Cattafesta, M. Sheplak, Ann. Rev. Fluid Mech. 2011, 43, 247.
- [3] S. Sultan, N. Hynes, Expert Rev. Med. Devices. 2015, 12, pp. 217-221.
- [4] J. F. LaDisa, I. Guler, L. E. Olson, D. A. Hettrick, J. R. Kersten, D. C. Warltier, P. S. Pagel, Ann. Biomed. Eng. 2003, 31, 972.
- [5] S. Kang, H. Choi, Phys. Fluids 2000, 12, 3301.
- [6] R. Nakanishi, H. Mamori, K. Fukagata, Int. J. heat fluid flow 2012, 35, 152.
- [7] H. Bai, Y. Zhou, W. G. Zhang, S. J. Xu, Y. Wang, R. A. Antonia, J. Fluid Mech. 2014, 750, 316.
- [8] B. H. Kim, et al., Nature 2021, 597, 503.
- [9] Y. Dong, L. Wang, N. Xia, Z. Yang, C. Zhang, C. Pan, D. Jin, J. Zhang, C. Majidi, L. Zhang, Sci. Adv. 2022, 8, eabn8932.
- [10] V. Iyer, H. Gaensbauer, T. L. Daniel, S. Gollakota, Nature 2022, 603, 427.
- [11] H.-J. Yoon, G. Lee, J.-T. Kim, J.-Y. Yoo, H. Luan, S. Chen, S. Kang, H. L. T. Huynh, H. Kim, J. Park, J. Kim, S. S. Kwak, H. Ryu, J. Kim, Y. S. Choi, H.-Y. Ahn, J. Choi, S. Oh, Y. H. Jung, M. Park, W. Bai, Y. Huang, L. P. Chamorro, Y. Park, J. A. Rogers, Sci. Adv. 2022, 8. eade3201.
- [12] J.-T. Kim, H. J. Yoon, S. Cheng, F. Liu, S. Kang, S. Paudel, D. Cho, H. Luan, M. Lee, G. Jeong, J. Park, Y.-T. Huang, S. E. Lee, M. Cho, G. Lee, M. Hang, B. H. Kim, J. Yan, Y. Park, S. Jung, L. P. Chamorro, J. A. Rogers, PNAS Nexus 2024, 3, pgae110.
- [13] G. Brennan, J. Gajjar, R. Hewitt, J. Fluid Mech. 2021, 909, A16.
- [14] G. B. Schubauer, H. K. Skramstad, Laminar-Boundary-Layer Oscillations and Transition on a Flat Plate, Vol. 909, NACA, Washington, DC 1943.
- [15] C. Kim, W.-P. Jeon, J. Park, H. Choi, Phys. Fluids 2003, 15, 265.
- [16] B. Gibeau, S. Ghaemi, Phys. Rev. Fluids 2022, 7, 114101.

- [17] H. Viets, M. Piatt, M. Ball, J. Wind Eng. Ind. Aerodynam. 1981, 7, 135.
- [18] P. Xavier, A. Ghani, D. Mejia, M. Miguel-Brebion, M. Bauerheim, L. Selle, T. Poinsot, J. Fluid Mech. 2017, 813, 127.
- [19] C. Thill, J. Etches, I. Bond, K. Potter, P. Weaver, Aeronaut. J. 2008, 112, 117,
- [20] K. Liu, F. Hacker, C. Daraio, Science Robotics 2021, 6, eabf5116.
- [21] J. H. Pikul, S. Li, H. Bai, R. T. Hanlon, I. Cohen, R. F. Shepherd, Science 2017, 358, 210.
- [22] Y. Yan, T. Wang, R. Zhang, Y. Liu, W. Hu, M. Sitti, Science Advances 2023 9 eadi3979
- [23] S. Park, E. Park, M. Lee, S. Lim, ACS Appl. Mater. Interfaces 2023, 15, 49843.
- [24] D. Melancon, B. Gorissen, C. J. García-Mora, C. Hoberman, K. Bertoldi, Nature 2021, 592, 545.
- [25] L. Ren, B. Li, Y. He, Z. Song, X. Zhou, Q. Liu, L. Ren, ACS Appl. Mater. Interfaces 2020, 12, 15562.
- [26] H. Kim, S.-K. Ahn, D. M. Mackie, J. Kwon, S.-H. Kim, C. Choi, Y. H. Moon, H. B. Lee, S. H. Ko, Mater. Today 2020, 41, 243.
- [27] E. Hajiesmaili, D. R. Clarke, Nat. Commun. 2019, 10, 183.
- [28] H. Fu, K. Nan, W. Bai, W. Huang, K. Bai, L. Lu, C. Zhou, Y. Liu, F. Liu, J. Wang, M. Hang, Z. Yan, H. Luan, Y. Zhang, Y. Zhang, J. Zhao, X. Cheng, M. Li, J. W. Lee, Y. Liu, D. Fang, X. Li, Y. Huang, Y. Zhang, J. A. Rogers, Nat. Mater. 2018, 17, 268.
- [29] Y. Li, Y. Zhao, Y. Chi, Y. Hong, J. Yin, Mater. Today Energy 2021, 22, 100874.
- [30] Y. Bai, H. Wang, Y. Xue, Y. Pan, J.-T. Kim, X. Ni, T.-L. Liu, Y. Yang, M. Hang, Y. Huang, J. A. Rogers, X. Ni, Nature 2022, 609 701
- [31] X. Ni, H. Luan, J.-T. Kim, S. I. Rogge, Y. Bai, J. W. Kwak, S. Liu, D. S. Yang, S. Li, S. Li, Z. Li, Y. Zhang, C. Wu, X. Ni, Y. Huang, H. Wang, J. A. Rogers, Nat. Commun. 2022, 13, 5576.
- [32] A. P. Iakovlev, A. S. Erofeev, P. V. Gorelkin, Biosensors 2022, 12, 956.
- [33] D. Mark, S. Haeberle, G. Roth, F. Von Stetten, R. Zengerle, Microfluidics Based Microsyst. 2010, 305-376.
- [34] R. R. Soares, A. S. Akhtar, I. F. Pinto, N. Lapins, D. Barrett, G. Sandh, X. Yin, V. Pelechano, A. Russom, Lab on a Chip 2021, 21, 2932.
- [35] E. Stamhuis, W. Thielicke, J. Open Res. Soft. 2014, 2, 30.
- [36] S. Ha, J. Park, D. You, Comp. Phys. Commun. 2021, 265, 107999.
- [37] B. Gibeau, S. Ghaemi, J. Fluid Mech. 2023, 966, A6.
- [38] I. Jacobi, B. McKeon, J. Fluid Mech. 2011, 688, 258.
- [39] Y. Qi, S. Tan, N. Corbitt, C. Urbanik, A. K. Salibindla, R. Ni, Nat. Commun. 2022, 13, 469.
- [40] J.-T. Kim, Y. Jin, L. P. Chamorro, J. Fluids Struct. 2019, 87, 319.
- [41] I. Marusic, D. Chandran, A. Rouhi, M. K. Fu, D. Wine, B. Holloway, D. Chung, A. J. Smits, Nat. Commun. 2021, 12, 5805.
- [42] A. Panina, A. Kosinov, Y. G. Yermolaev, V. Gorev, N. Semionov, Thermophys. Aeromech. 2014, 21, 3.
- [43] A. M. Hamed, A. Kamdar, L. Castillo, L. P. Chamorro, Phys. Fluids 2015, 27, 10.
- [44] T. Kim, G. Blois, J. L. Best, K. T. Christensen, J. Fluid Mech. 2020, 887. A3.
- [45] C. Seol, T. Kim, T. Kim, J. Fluid Mech. 2024, 985, A29.
- [46] M. Itoh, S. Tamano, K. Yokota, S. Taniguchi, J. Turbulence 2006, N27.
- [47] H. Abe, H. Kawamura, Y. Matsuo, J. Fluids Eng. 2001, 123, 382.